Korean J. Chem. Eng., 40(12), 2787-2799 (2023)
DOI: 10.1007/s11814-023-1528-6

pISSN: 0256-1115
eISSN: 1975-7220

Study of the influence of operational parameters on biomass conversion in a pyrolysis reactor via CFD

Alysson Dantas Ferreira*,†, Suzana Dantas Ferreira,‡, and Severino Rodrigues de Farias Neto*,‡**

*Process Engineering, UFCG, Aprigio Veloso, 882, Campina Grande, 58429900, PB, Brazil
**Mechanical Engineering, UFCG, Aprigio Veloso, 882, Campina Grande, 58429900, PB, Brazil
(*Received 16 January 2023 • Revised 3 June 2023 • Accepted 10 July 2023*)

Abstract−Pyrolysis has been one of the technologies used to convert biomass into biofuels. Therefore, mathematical models that can represent its phenomena are of fundamental importance in understanding the reaction progression and optimizing the process. In this sense, this study compared the results obtained from the lumped-capacitance thermal model proposed in this work with the thermal discretization model that considers thermal conductivity as a function of temperature. Then, the effect of operational parameters such as temperature, gas velocity, and biomass particle diameter, was compared on the reaction conversion rate. To describe the behavior and interaction between the phases, we utilized an Eulerian-Lagrangian CFD modeling approach, solving the continuity, momentum, energy, species, and turbulence equations using OpenFOAM. A factorial design of the type 2^k was used to manipulate the model's input parameters, with biomass conversion as the response variable. The numerical results of biomass conversion from the lumped-capacitance model showed good agreement with the data reported in the literature for the discretized model. However, we observed a difference of 9.13% in the particle mass behavior and 7.63% in the particle residence time. The design of experiments (DoE) enabled us to determine the impact of individual parameters and their interactions on the pyrolysis conversion rate with temperature identified as the most sensitive parameter. Therefore, despite the observed errors when comparing the two models, the lumped-capacitance model accurately represented the reaction yields and proved to be suitable for simulations involving a large number of particles, facilitating optimization studies.

Keywords: Modeling, Simulation, CFD, DoE, Optimization

INTRODUCTION

Extreme weather events have become increasingly frequent, as seen in the news, and are causing severe consequences for both human populations and natural ecosystems. This has intensified the debate on global warming and has led countries to take action to combat climate change. One of the main goals of this agenda is to reduce the emissions of gases that cause the greenhouse effect through long-term strategic actions.

Carbon dioxide CO_2 is the main gas that causes the greenhouse effect. It is emitted into the atmosphere by burning fossil fuels used in the most diverse human activities. Therefore, minimizing these emissions is significant to curb global warming. Although fossil fuels have historically been the primary energy source, there are now more attractive alternatives such as renewable energy sources that produce significantly less toxic pollutants and also reduce carbon dioxide emissions [1].

Biomass has received significant attention as a renewable energy resource to produce bioenergy and biofuels, approaching various energy and environmental issues due to the use of fossil fuels [2]. According to the World Energy Resources report (2016) prepared by the World Energy Council, the energy generated from biomass, known as bioenergy, is currently the largest renewable source in the world, accounting for 14% of renewable energies and 2% of global production. Furthermore, the World Bioenergy Association estimates that the use of biomass could be increased by up three times by 2035 when renewable sources could reach more than 50% of the world's energy demand.

There are a series of processes to convert biomass into fuels, which can be physical, thermochemical, and biochemical. Within thermochemical, pyrolysis has been one of the most favorable for producing tar [1]. In this process, biomass is thermally degraded in an inert atmosphere (in the absence of oxygen) and at moderate temperatures, taking just a few seconds for its decomposition [1]. Pyrolysis takes place in two main steps. The primary products of biomass particle degradation are generally referred to as tar, gas, and char. The produced tar secondary reaction results in the formation of secondary degradation products and, naturally, reducing organic yields [3-5].

There is a vast amount of experimental studies on the biomass pyrolysis field [6]. However, even if the experiments help optimize the pyrolysis process, Duarte et al. [7] show that applying experimental techniques may find some obstacles, such as the cost of building equipment, disturbances caused by intrusive experimental measures, among others. In this way, applying numerical simulation may contribute to the complex physics deep understanding of pyrolysis's thermochemistry by helping to develop and optimize equipment.

†To whom correspondence should be addressed.
E-mail: alysson.dantas@eq.ufcg.edu.br
‡These authors contributed equally to this work.

Most CFD works reported in the literature are applications of biomass pyrolysis in fluidized bed reactors [8]. In the works carried out by Papadikis et al. [9-11] and Papadikis et al. [12,13] the effect of sphericity, particle drag, and the influence of particle size on heat transfer, momentum, mass, and chemical species were simulated in a fluidized bed. Hu et al. [14] modeled the fast pyrolysis reaction using CFD-DEM to investigate the effects of particle shrinkage and gas velocity. Their results indicate that the shrinkage has a negligible impact on the product yield, but it significantly affects the drag behavior. Park and Choi [15] analyzed the influence of reaction temperature and gas velocity on hydrodynamics, heat transfer, and pyrolysis. They identified a significant change in the pyrolysis product yield due to increased mixing and heat transfer, increasing gas velocity. Yang et al. [6] modeled a three-dimensional bubbling fluidized bed (BFB) reactor for fast pyrolysis using the MPPIC method of the Euler-Lagrange approach to study the physical and thermal dynamics of bubbles under the condition of high temperature. Their results indicated that the axial segregation induced by the difference in size and density between sand and biomass results in the preferential distribution of biomass particles, significantly affecting the hydrodynamic, thermal, and chemical species distributions. According to Papadikis et al. [10], single particle models can provide a good view of how the progress of the pyrolysis reaction is controlled and also predicts accurate conversion and product yields.

Therefore, the objective of this study is to compare the results obtained from the lumped-capacitance thermal model, which assumes uniform temperature throughout the system, with the thermal discretization model that takes into account the thermal conductivity as a function of temperature. By identifying the differences between these two models, we aim to assess their effectiveness in predicting pyrolysis behavior. Subsequently, the lumped-capacitance model will be applied to investigate the effects of temperature, gas velocity, and biomass particle diameter on the pyrolysis conversion rate. These parameters will be measured in an experimental design, providing valuable insights into the relationship between these factors and the pyrolysis process.

MATHEMATICAL MODELING

Four equations describe the gas phase in a dense gas-solid reactive flow: the continuity equation, the momentum equations, the energy equation, and the species equation. As we will see next, there is a term that represents the volumetric gas fraction (α_g) and is calculated by:

$$\alpha_g = 1 - \alpha_p \tag{1}$$

where α_p is the volumetric fraction of the solid phase, given by:

$$\alpha_g = \frac{1}{V_{elem}} \sum_{i=1}^{n} W_{p,i} V_{p,i} \tag{2}$$

$W_{p,i}$ is the portion of the particle volume occupied in the current mesh element, where $V_{p,i}$ is the particle volume and V_{elem} is the mesh element volume.

The discrete particle model (DPM) was used with the soft sphere collision model for the particulate phase. In this approach, it is considered that the particles undergo a small deformation during contact.

The equations that model both phases will be presented below.

1. Gas Phase

The continuity equation of gas phase can be formulated as:

$$\frac{\partial(\alpha_g \rho_g)}{\partial t} + \nabla \cdot (\alpha_g \rho_g \mathbf{u}_g) = \delta \dot{m}_s \tag{3}$$

where α_g, ρ_g, and $\mathbf{u}_g$ are the volume fraction, density, and velocity, respectively. $\delta \dot{m}_s$ represents the source term that models the chemical reactions between phases.

The term $\delta \dot{m}_s$ in Eq. (3) represents the rate of mass consumption or generation caused by the interaction between the gas phase and the particulate phase, calculated by:

$$\delta \dot{m}_s = \frac{1}{V_{elem}} \sum_{i=0}^{N_p} W_{p,i} \chi_{t,i} \tag{4}$$

$\chi_{t,i}$ are all the mass transfer terms between the gas phase and particulate phase that are acting on particle i.

The momentum equation of gas phase can be written as:

$$\frac{\partial(\alpha_a \rho_g \mathbf{u}_g)}{\partial t} + \nabla \cdot (\alpha_g \rho_g \mathbf{u}_g \mathbf{u}_g) = -\alpha_g \nabla p_g + \rho_g \alpha_g \mathbf{g} + \nabla \cdot (\alpha_g \boldsymbol{\tau}_g) + \mathbf{F}_{gs} \tag{5}$$

Where p_g and $\mathbf{g}$ are the gas pressure and gravitational acceleration terms, respectively. The term $\boldsymbol{\tau}_g$ represents the stress tensor calculated by:

$$\boldsymbol{\tau}_g = (\mu_l + \mu_t)(\nabla \mathbf{u} + (\nabla \mathbf{u})^T) - \frac{2}{3}(\mu_l + \mu_t)(\nabla \cdot \mathbf{u})\mathrm{I} \tag{6}$$

where μ_l and μ_t are the laminar and turbulent viscosity, respectively. The turbulent viscosity is calculated using the Smagorinsky model [16], which for large turbulent structures are solved directly while small ones are modeled by:

$$\mu_t = C \rho_g \Delta^2 \sqrt{\left(\frac{\partial u_i}{\partial x_j} + \frac{\partial u_j}{\partial x_i}\right)^2} \tag{7}$$

where Δ is the characteristic length, equal to the cube root of the volume of the element, $\Delta = (\Delta x \Delta y \Delta z)^{1/3}$. C is the Smagorinsky constant, given as 0.01. The term $\mathbf{F}_{gs}$ in Eq. (5) represents the exchange of momentum between the solid and gas phases and can be calculated by:

$$\mathbf{F}_{gs} = \frac{1}{V_{elem}} \sum_{i=0}^{N_p} W_{p,i} \mathbf{f}_{t,i} \tag{8}$$

where $\mathbf{f}_{t,i}$ are all the fluid-particle interaction forces acting on particle i.

The energy equation of gas phase in term of enthalpy can be written as:

$$\frac{\partial(\alpha_g \rho_g h_g)}{\partial t} + \nabla \cdot (\alpha_g \rho_g \mathbf{u}_g h_g) = \alpha_g \left(\frac{\partial p_g}{\partial t} + \mathbf{u}_g \cdot \nabla p_g\right) - \nabla \cdot (\alpha_g q) + \dot{Q}_D + Q_{gs} + Q_{gw} - \Delta H_{rg} + Q_{rad} \tag{9}$$

where h_g and ΔH_{rg} are the enthalpy and heat of chemical reaction, respectively. The enthalpy is calculated by adding the enthalpy of each species (h_g):

$$h_g = \sum_{k=1}^{N_k} h_g^k Y_g^k = \sum_{k=1}^{N_k} Y_g^k \left(\int_{T_0}^{T_g} C_p^k dT + \Delta h_g^k \right) \quad (10)$$

where N_k is the number of chemical species present in the gaseous phase. T_0, T_g, C_p^k and Δh_g^k are respectively the reference temperature, the gas phase temperature, the specific heat of the species k and the heat of reaction. Q_{gs} and Q_{gw} represent the heat transfer terms between gas-solid and gas-wall, respectively. The convective heat transfer between the wall and the gas phase (Q_{gw}) is calculated by:

$$Q_{gw} = h_{gw} A_{gw} (T_w - T_g) \quad (11)$$

where T_w and A_{gw} are the temperature and surface area of the wall, respectively. The convection heat transfer coefficient h_{gw} is calculated by:

$$h_{gw} = \frac{N_u \lambda_g}{L} \quad (12)$$

where N_u is the Nusselt number, and L is the characteristic length. $\dot{Q}_D$ is the enthalpic diffusion calculated by:

$$\dot{Q}_D = \sum_{k=1}^{N_k} \nabla \cdot (\alpha_g h_g^k \rho_g D_{if,g}^k \nabla Y_g^k) \quad (13)$$

The heat flux q is calculated by:

$$q = \lambda_g \nabla T_g \quad (14)$$

where the term λ_g is the thermal conductivity of the gas phase and includes the molecular (or laminar) λ_l and turbulent (λ_t) conductivity terms. λ_g is calculated by:

$$\lambda_g = \frac{C_p \mu_t}{Pr_t} \quad (15)$$

where Pr_t is the Prandtl turbulent number. The term Q_{gs} in Eq. (9) represents the heat exchange between the gas phase and the solid phase, calculated by:

$$Q_{gs} = \frac{1}{V_{elem}} \sum_{i=0}^{N_p} W_{p,i} Q_{t,i} \quad (16)$$

where $Q_{t,i}$ represents all the heat transfer terms between the gas phase and the particulate phase that are acting on particle i.

The transportation equation of gas species can be formulated as:

$$\frac{\partial(\alpha_g \rho_g Y_g^k)}{\partial t} + \nabla \cdot (\alpha_g \rho_g \mathbf{u}_g Y_g^k) = \nabla(\alpha_g \rho_g D_{if,g}^k \nabla Y_g^k) + \dot{m}_{react,g}^k + \dot{m}_{react,gs}^k \quad (17)$$

This equation is solved based on the chemical species k, and each computational element is summed to obtain the species change of the gaseous mixture. $D_{if,g}^k$ is the turbulent mass diffusivity calculated by:

$$D_{if,g}^k = \frac{\mu_g}{\rho_g S_c} \quad (18)$$

where μ_g is the viscosity of the gas and S_c is the Schmidt number, which for this work was considered 0.9. $\dot{m}_{react,g}^k$ models the chemical reactions of the gas phase for each chemical species. This term is calculated by:

$$\dot{m}_{react,g}^k = k_i C_i \quad (19)$$

where k_i and C_i are the reaction rate constant and the concentration of component i, respectively. The reaction rate constant will be detailed in section 2.4.

The term $\dot{m}_{react,gs}^k$ in Eq. (17) represents the rate of consumption or generation of species k caused by the interaction between the gas phase and the particulate phase, calculated by:

$$\dot{m}_{react,gs}^k = \frac{1}{V_{elem}} \sum_{i=0}^{N_p} W_{p,i} \chi_{t,i}^k \quad (20)$$

$\chi_{t,i}^k$ represents all the chemical species transfer terms between the gas phase and the particulate phase that are acting on particle i.

2. Solid Phase

The motion of the particle i of mass m_i and volume V_i in a system is calculated according to Newton's second law of motion given by:

$$m_i = \frac{d\mathbf{u}_{s,i}}{dt} = m_i \frac{d^2 \boldsymbol{\xi}_i}{dt^2} = f_i^{g\text{-}s} + f_i^{s\text{-}w} + f_i^{grav} \quad (21)$$

where $\mathbf{u}_{s,i}$ is the velocity, $\boldsymbol{\xi}_i$ is the position of particle i, $f_i^{g\text{-}s}$ represents the forces acting on the particles due to interaction with fluids, f_i^{grav} is gravity force on particle i and $f_i^{s\text{-}w}$ is the particle-wall collision term.

The angular momentum of a given particle i is calculated by:

$$\mathbf{I}_i \frac{d\omega_i}{dt} = \mathbf{M}_i^{g\text{-}s} \quad (22)$$

$\mathbf{M}_i^{g\text{-}s}$ is the torque caused by the fluid-particle effect. $\mathbf{I}_i$ is the moment of inertia, which for a spherical particle of radius r_i is calculated by $\mathbf{I}_i = \frac{2}{5} m_i r_i^2$.

Each particle assumes to have a uniform temperature, and thus the conservation of energy of particle i in a system is calculated by:

$$m_i c_{p,i} = \frac{dT_i}{dt} = Q_{gs} + Q_{rad} + \Delta H_{rs} \quad (23)$$

where $c_{p,i}$ and T_i is the heat capacity and temperature of particle i, Q_{gs} is the net heat by the interaction between the gas phase and the particle phase, calculated by:

$$Q_{gs} = \frac{\lambda_g Nu_i}{d_s} A_i (T_g - T_s) \quad (24)$$

where d_s and A_i is the diameter and surface area of the particle. Nu_i is the Nusselt number of the particle calculated by:

$$Nu_i = 2 + 0.6 Re_s^{0.5} P_r^{0.33} \quad (25)$$

where P_r and Re_s are the particle's Prandtl numbers and Reynolds numbers, respectively. ΔH_{rs} is the heat of reaction of the solid phase, and Q_{rad} is the effect of radiation on the particle, calculated by:

$$Q_{rad} = \sigma \varepsilon_s A_s (T_{b,local}^4 - T_s^4) \quad (26)$$

where σ and ε_s are the Stefan-Boltzmann constant and the emissivity of the particle.

The following equation calculates the mass of each particle i in a system:

$$\frac{dm_i}{dt} = \sum \Omega_i \tag{27}$$

Ω_i represents the mass source term that can increase or decrease due to the chemical reaction of the solid phase.

The following equation calculates the composition of each particle i present in a system:

$$\frac{d(m_i Y_{i,k})}{dt} = \sum \Omega_{i,k} \tag{28}$$

$Q_{i,k}$ represents the source term of the chemical species present in the particles that can increase or decrease due to a chemical reaction.

3. Gas-particle Interaction

The drag model is vital in describing a gas-particle system, representing the momentum exchange between phases. The drag force of a single particle i is given by:

$$\mathbf{f}_i^{g-s} = \mathbf{f}_{D,i} = \frac{V_p D_p}{1-\alpha_g}(\mathbf{u}_g - \mathbf{u}_{s,i}) \tag{29}$$

The Gidaspow drag model combines the Ergun correlation applicable for dense systems [17] with the Wen-Yu correlation used for dilute systems [18] is appropriate for most gas-solid modeling. The Gidaspow model is written as follows:

$$D_p = \begin{cases} \dfrac{150(1-\alpha_g)^2 \mu_g}{\alpha_g d_p^2} + \dfrac{1.75\rho_g(1-\alpha_g)|\mathbf{u}_g - \mathbf{u}_{s,i}|}{d_p}, & \alpha_g \le 0.8 \\ \dfrac{3}{4}\dfrac{\alpha_g \rho_g (1-\alpha_g)|\mathbf{u}_g - \mathbf{u}_{s,i}|}{d_p} C_D \alpha_g^{-2.65}, & \alpha_g > 0.8 \end{cases} \tag{30}$$

where

$$C_D = \begin{cases} \dfrac{24}{Re_s}(1 + 0.15 Re_s^{0.687}), & Re_s < 1000 \\ 0.44, & Re_s \ge 1000 \end{cases} \tag{31}$$

and

$$Re_s = \frac{\rho_g \alpha_g |\mathbf{u}_g - \mathbf{u}_{s,i}| d_p}{\mu_g} \tag{32}$$

The force of gravity acting on the particle is given by:

$$f_i^{grav} = \frac{\mathbf{g}(\rho_g - \rho_s)}{\rho_g} \tag{33}$$

where ρ_s is the density of particle i and **g** is the gravity acceleration.

4. Kinetics

The fast pyrolysis of biomass, which occurs in reactors, involves many elementary reactions [19,20]. As a result, biomass tar produces several chemical products, such as organic acid compounds, ketones, and phenols. In addition, some synthesis gas hydrocarbons were found in the gas compounds such as CH_4, CO_2, CO, H_2 and other synthesis gas hydrocarbons [21]. However, the detailed kinetics of the reaction and the fundamental mechanisms of decomposition are still being studied, as these are complex chemical reactions, and the information on intermediate species is still unclear [18].

In CFD studies, chemical reactions are reduced to a set of main reactions that describes the pyrolysis process. Fig. 1 presents the two-step kinetic mechanism used in this work. This mechanism has already been used, showing satisfactory results [15,22]. In this kinetics, the primary reaction is the decomposition of biomass material (Wood) into gas, char, and tar. Subsequently, the tar will be decomposed into gas, and char [23].

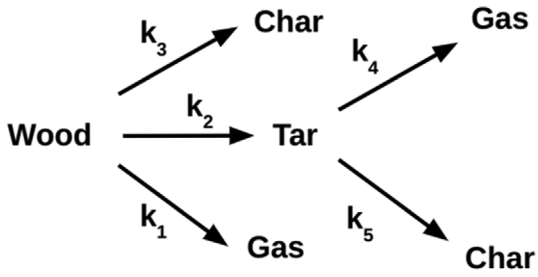

Fig. 1. Two-stage, semi-global reaction mechanism of the pyrolysis reaction [11].

Table 1. Arrhenius parameters for the pyrolysis reaction

Reactions	γ_i [s^{-1}] [24]	E_i [J/kmol] [24]
Reaction 1 (k_1)	1.30e8	1.40e8
Reaction 2 (k_2)	2.00e8	1.33e8
Reaction 3 (k_3)	1.08e7	1.21e8
Reaction 4 (k_4)	1.48e6	1.44e8
Reaction 5 (k_5)	1.48e6	1.44e8

Arrhenius' law is used to calculate the rate of the chemical reaction and can be formulated as follows:

$$k_i = \gamma_i \exp\left(\frac{-E_i}{RT}\right) \tag{34}$$

where R is the universal gas constant, γ_i is the pre-exponential factor and E_i is the activation energy. Table 1 details the kinetic parameters of the reaction. These parameters were obtained by Chan et al. [24]. The pyrolysis reaction is exothermic, and ΔH_r is −255 kJ/kg. The kinetic parameters of pyrolysis depend on the biomass properties, such as the heating rate and measurement approach. In contrast, the geometric configuration of the reactor has a negligible influence on the chemical kinetics of biomass pyrolysis [24].

SIMULATION SETUPS

The present work was based on a study conducted by Papadikis et al. [11]. In order to speed up simulations without compromising the quality of the results, it was decided to simplify the geometry of Papadikis et al. [11] to a pseudo-2D format with 7 mm thickness. This simplification was inspired by the work of Li et al. [25], where they concluded that the bed thickness should be at least 12.3 times the particle size to neglect the wall effect and ensure it does not influence particle behavior.

The accuracy of a CFD solution is directly influenced by the number of elements in the mesh. Generally, a higher number of elements leads to better simulation accuracy. However, increasing mesh refinement also results in higher computational processing costs and longer calculation times [26]. Therefore, it is recommended to perform

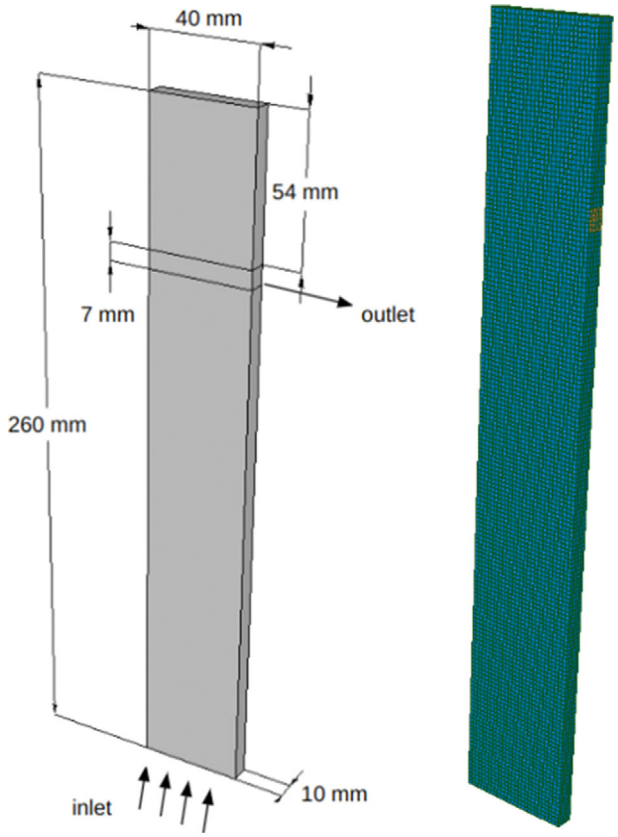

Fig. 2. Fluidised bed geometry and mesh.

a mesh dependency analysis for CFD studies. This involves simulating the study with various mesh element sizes to determine the minimum number of elements required to obtain accurate results while minimizing computational costs. However, in CFD simulations employing the Eulerian-Lagrangian approach solved by the Discrete Phase Model (DPM) method, there is a particular consideration to be taken into account. The mesh element size is limited by the particle size, which must be sufficiently small to achieve accuracy and, at the same time, large enough to ensure a proper temporal and spatial variation of the solid particle fractions [27]. it is common to follow recommendations from previous studies [27].

Based on the information presented, the findings of Peng et al. [28] suggest that the ratio between element size (S_c) and particle size (d_p) should be greater than 1.6 to ensure accurate predictions. Clarke et al. [29] also observed that ratios (S_c/d_p) below 1.6 resulted in poor predictions for particulate flow. Additionally, Boyce et al. [30] recommended a ratio (S_c/d_p) around 3-4 for achieving the best agreement between experimental and numerical data in fluidized bed problems. Therefore, in this study, we followed these recommendations and used a ratio (S_c/d_p) of 3. Consequently, the computational mesh was composed of 27 x 4 x 174 elements in the x, y, and z directions. The study domain and the computational mesh are illustrated in Fig. 2.

The models presented in this work were implemented in OpenFOAM-v2012, an open-source program. Taking advantage of this characteristic, the reactingParcelFoam solver was modified, which is used to solve transient problems with compressible, turbulent flow,

Table 2. Simulation parameters

Simulation parameters	Values
ρ_{wood}	700 kg/m^3
$\rho_{N_2,\,tar,\,gas}$	Ideal gas
d_p	0.05e-2 m
T_p	303 K
$T_{0,\,reactor}$	303 K
T_{N_2}	773 K
$u_{0,\,p}$	0 m/s
$u_{0,\,reactor}$	0 m/s
$u_{N_2,\,inlet}$	1.2 m/s
P_{outlet}	101,325 Pa
$\mu_{N_2,\,tar,\,gas}$	3e-5 Pa s
λ_{wood}	0.12 W/mK
λ_{char}	0.071 W/mK
λ_{N_2}	3.58e-2 W/mK
$\lambda_{tar,\,gas}$	2.577e-2 W/mK
$c_{p,\,wood}$	1,500 J/kgK
$c_{p,\,char}$	670 J/kgK
$c_{p,\,N_2}$	1,121 J/kgK
$c_{p,\,tar}$	2,500 J/kgK
$c_{p,\,gas}$	1,100 J/kgK

chemical reaction, and multiphase. The code was modified to include the DPM model, considering the volumetric fraction effects of the particles in the continuous phase and the collisions of particles/walls. Subsequently, the sub-models of the kinetics of heterogeneous pyrolysis reactions were implemented in the software's source code.

In this study, the inlet flow consists only of nitrogen, which enters the reactor from the base at a fixed velocity of 1.2 m/s and a temperature of 773 K. The reactor outlet was set at atmospheric pressure, and the walls were assumed to be non-slip and adiabatic. Initially, the reactor was filled with stagnant N_2 at a temperature of 303 K. The biomass particle is inserted into the center of the reactor at the height of 0.0135 m, with a velocity of 0 m/s and a temperature of 303 K. The particle has a diameter of 500 μm, and its thermal conductivity and specific heat are proportionally calculated based on the solid mass fraction (wood and char). As the particle is heated, the biomass undergoes degradation into char, tar, and gas. The properties of N_2, pyrolysis gases, and biomass are shown in Table 2.

The equations were solved using the finite volume method (FVM). In this approach, the transient term was discretized using the second-order Crank-Nicolson scheme, while the convection and diffusion terms were discretized using the Upwind and Gauss linear schemes, respectively. These discretization schemes were chosen because they demonstrated numerical stability in solving the linear matrix.

The result of the discretization is a set of algebraic equations constructed in the form $A[\phi]=b$. The coefficients of the unknown variables in matrix A are obtained through the linearization procedure of the information within the computational mesh. Vector b contains all the source terms, including constants, boundary conditions, and non-linearizable components. The techniques for solving this

algebraic system are not dependent on the specific discretization method employed. In this study, the GAMG method was used for solving the pressure field, the smoothSolver for the velocity field, and the PBiCGStab for the other fields.

To calculate the velocity and pressure fields, Eq. (3) needs to be coupled with Eq. (5). This coupling is achieved using a pressure-velocity coupling algorithm. In this work, a hybrid algorithm based on PISO and SIMPLE, called PIMPLE, was adopted, following the recommendation of Xiong et al. [31]. According to the authors, this algorithm allows for relatively large time steps while maintaining numerical stability and avoids pressure checkerboarding.

Each case is simulated for a physical time of 4s, with a varied time step and a Courant number fixed at 0.5. The simulations were performed on a computer with an Intel core i9-12900k processor and 32 Gb of RAM, taking 1.2 h to be completed, using two processing cores.

DESIGN OF NUMERICAL EXPERIMENTS

Design of Experiments (DoE) is a statistical branch used to plan experiments, that is, a tool that defines what information, in what quantity, and under what conditions the results of experiments should be collected. It allows various input parameters of experiments to be manipulated, determining their effect on a specified response variable, and providing a wealth of information about their interactions. Therefore, this technique is recommended for studying how factors influence the variable of interest behavior.

This methodology can be extrapolated and applied to design numerical simulations, and when this occurs, it is called design of numerical experiments. The conversion of biomass into products was defined as the response variable, and the parameters of interest studied were the inert gas's velocity, the gas's temperature, and the diameter of the biomass particle. A numerical experimental design of the type 2^k was carried out with the variations of the factors as shown in Table 3.

The R software processed the data obtained from the configuration presented in Table 3.

RESULTS

1. Validation

During the pyrolysis process, biomass particles are heated in an inert atmosphere, initiating chemical reactions. For the single particle case, the physical phenomenon is the same. To verify if the heat and mass transfer models adopted in this work may describe the pyrolysis physics, the temperature behavior, mass variation, density, and reaction yields for biomass, biochar, biogas, and the bio-oil vapor was studied, and the results were compared to the data obtained by Papadikis et al. [11] and will be presented below.

1-1. Particle's Surface Temperature

The model used by Papadikis et al. [11] to represent the behavior of the biomass particle is presented in Eq. (35).

$$\frac{\partial}{\partial t}(\rho c_{p,i} T_i) = \frac{1}{r_i^2}\frac{\partial}{\partial r_i}\left(\lambda_i r_i^2 \frac{\partial T_i}{\partial r_i}\right) \tag{35}$$

This model discretizes the particle along its radius to obtain the biomass temperature at each point. Still analyzing Eq. (35), it is observed that the thermal conductivity of the particle varies with the radius, making it a temperature function, driving the model even more accurate.

The model used in this work (Eq. (23)) considers that the internal thermal resistance of the particle is negligible, and the temperature is uniform throughout the particle. However, this condition does not faithfully represent the reality of heat transfer in biomass since the particle's surface is heated more quickly, and the heat is conducted along the particle's radius more slowly. Furthermore, according to Norouzi et al. [32], an assumption like this can only be valid for tiny particles with the Biot number<0.1. Therefore, this value was calculated as shown in Table 4.

It is observed in Table 4 that the Biot number for the simulation is higher than recommended. Faced with the slight difference in Biot number value and the impossibility of changing the particle's diameter and conductivity, this error was incorporated in modeling, allowing a comparison with Papadikis et al. [11]. Resulting in faster biomass consumption, affecting the time the particle remains in the reactor. Assuming this behavior makes it impossible to accu-

Table 3. Simulations evaluated by factorial design 2^k

Simulation	u_g [m/s]	T_g [K]	d_p [m]
1	1.4	823	7.5e-4
2	1.4	823	2.5e-4
3	1.4	723	7.5e-4
4	1.4	723	2.5e-4
5	1.0	823	7.5e-4
6	1.0	823	2.5e-4
7	1.0	723	7.5e-4
8	1.0	723	2.5e-4

Table 4. Biot number of the simulation

Re_p [ ]	Pr [ ]	H [W/m^{2}K]	Bi [ ]
3.53	0.715	338.68	0.24

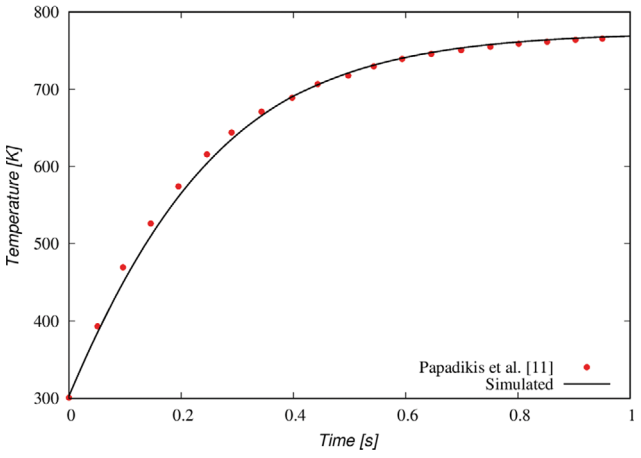

Fig. 3. Particle's surface temperature behavior during 1 second.

rately say the particle's residence time in the reactor. This consideration was also adopted in work by Papadikis et al. [9].

The simulation was performed according to the considerations mentioned above, and the particle temperature obtained was compared with the particle surface temperature reported by Papadikis et al. [11], as shown in Fig. 3. This comparison is valid because both models should present similar results on the particle surface.

Comparing the behavior of the simulation's temperature obtained with the result of the particle's surface temperature reported by Papadikis et al. [11], we observed a good agreement between the data, reinforcing that the model suggested by this research could capture the heat transfer between the fluid and the particle's surface.

When analyzing the temperature behavior, it is observed that it describes a flash-type pyrolysis behavior, which corroborates the statement by Batista Junior [33], as the heating rate is far above 100 K/s, value suggested by Batista Junior [33]. The biomass particle starts the process with an initial temperature of 300 K and reaches the inert atmosphere temperature of 773 K in just 1 second, with a heating rate of 473 K/s. After that time, the particle's temperature remains the value until the particle is dragged out of the fluidized bed reactor.

1-2. Particle Mass

Hydrocarbons' large and complex chains are decomposed during pyrolysis into smaller and simpler molecules, forming tar, gas, and char. When formed, tar and gas detach from the biomass as vapor, while the solid particle is transformed into char, joining the unreacted biomass composition. During this process, the particle's mass changes.

The results presented in Fig. 4 indicate that the particle mass behavior obtained by this work is similar to the behavior reported by Papadikis et al. [11]. The particle is being heated in the first 0.5 seconds, and the pyrolysis reactions are still starting, so a significant mass change is not observed. After this time, it is possible to follow mass dropping due to the reactional particle increase due to the temperature effect that drives the chemical reactions.

Still analyzing Fig. 4, we observe the effect that the temperature equation causes on the particle's mass. The results obtained by this work show that biomass is consumed faster than the data reported by Papadikis et al. [11]. This behavior is due to the consideration that the particle presents uniformity in temperature and thermal conductivity, causing a uniform reaction throughout the particle radius. While in the work of Papadikis et al. [11], the reaction is faster at the surface and slower at the center, leading to a slower biomass consumption and, consequently, a slower mass loss.

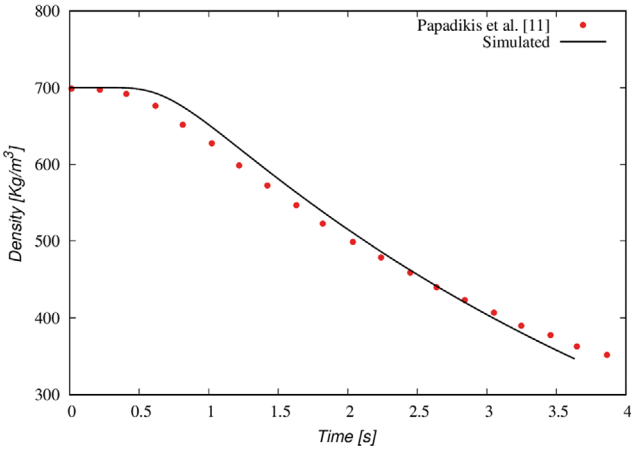

Fig. 4. The behavior of the particle mass during pyrolysis.

The biomass particle was carried out of the reactor at different times. In the present work, the particle leaves in 3.63 seconds with a mass of 2.19×10^{-8} kg while the particle of Papadikis et al. [11] exits in 3.93 seconds with a mass of 2.41×10^{-8} kg. The difference between the masses showed an error of 9.13%. The particle residence time in the reactor will be discussed in more detail below.

1-3. Particle Dynamics

The particle was inserted into the reactor at 0 seconds with a zero velocity at the height of 0.04 m. When gravity acts together with the particle's mass, not yet reacted, the weight force is greater than the drag force, causing the particle deposition at the reactor's bottom. Since entering the reactor, the biomass particle is being heated due to direct contact with the inert gas, taking approximately 1 second to reach the temperature of the control volume. At this moment, its reactivity becomes more intense, increasing the conversion of biomass into gas, tar, and char. This reaction causes the particle's mass reduction, changing the balance forces acting on it, and slowly, the weight force weakens in relation to the drag force. When the drag force becomes stronger than the weight force, the particle begins to be ejected out of the reactor. This behavior can be observed in Fig. 5.

The behavior observed in Fig. 5 is similar to the reported by Papadikis et al. [11]. However, in the present research, the particle was carried out of the reactor in 3.63 seconds, while the particle of Papadikis et al. [11] exits in time 3.93 seconds, an error of 7.63%. This disagreement is due to the different thermal models used in both works, which cause a consumption of the particle's mass at different speeds, affecting the behavior of the force acting on the particle and, consequently, causing them to be carried out of the reactor in times many different.

1-4. Particle Density

Papadikis et al. [11] consider in their work the particle is spherical, and there is no shrinkage in volume during pyrolysis. The present research also considered the shape of the spherical particle but worked with the particle shrinkage model presented in Eq. (36).

$$V_i = \frac{m_i}{\rho_i} \tag{36}$$

where m_i and ρ_i are the mass and density of the particle, respectively. ρ_i is given by the weighted average of the densities of the components that make up the particle. The results of the density behavior of both works are shown in Fig. 6.

When analyzing Fig. 6, we observe that the density behavior obtained by this work presents a good agreement with the result given by Papadikis et al. [11]. Although the mass reacted more quickly due to the effect of the model adopted for temperature, the variation in volume during pyrolysis adopted in this work ended up compensating for the behavior of the mass. It reduced the rate of decrease in density during pyrolysis. During the reaction, the particle loses mass and shrinks in size, making it lighter.

1-5. Relative Yield of the Pyrolysis Reaction

The relative yield quantifies the proportion of gas, tar, char, and

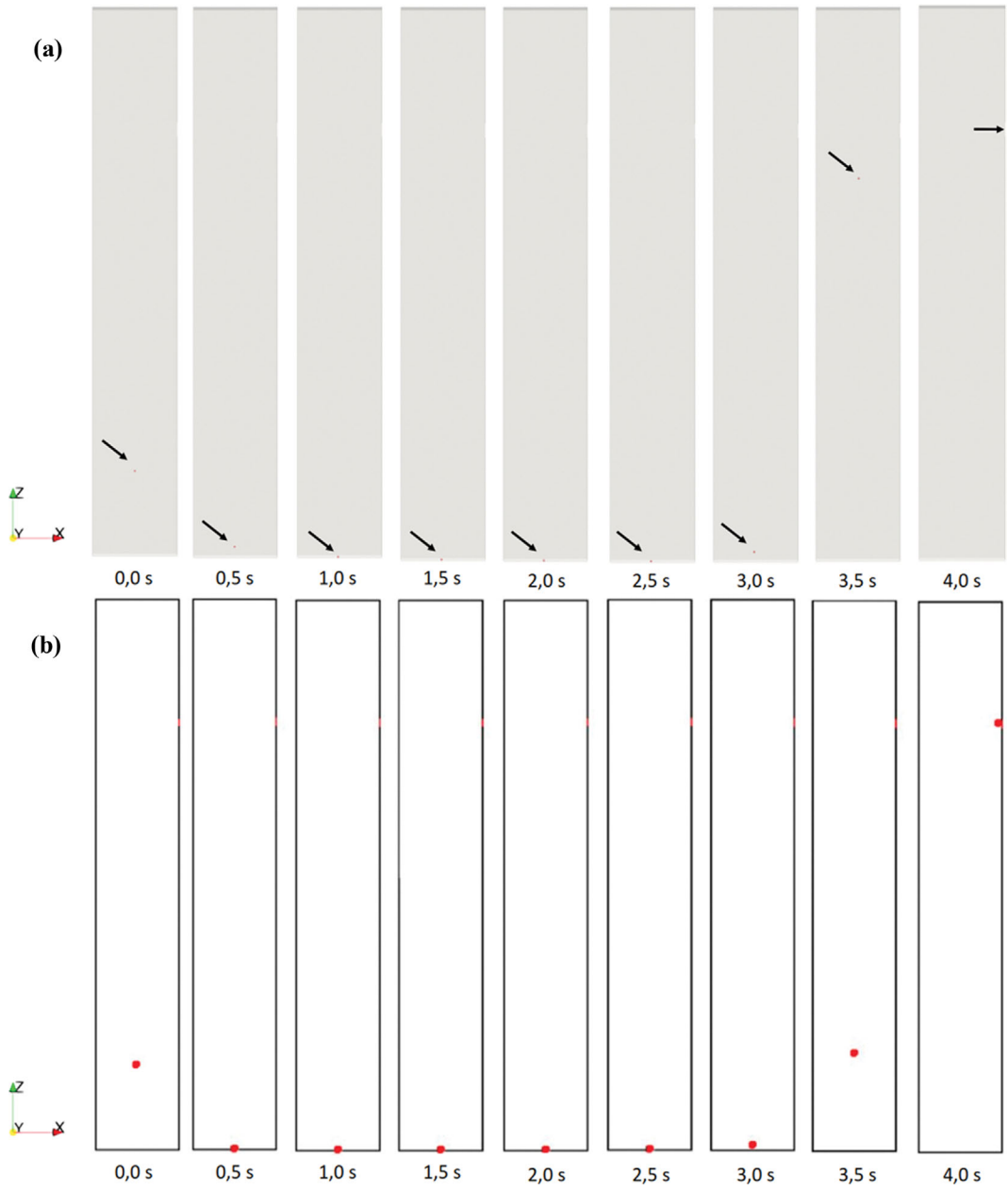

Fig. 5. Particle dynamics during the pyrolysis of (a) this work and (b) Papadikis et al. [11].

biomass formed at the end of the process compared to the sum of all products. The relative yield over time of the products formed by the pyrolysis reaction was calculated to validate the models that describe mass transfer behavior between phases. These results can be seen in Fig. 7.

As with any irreversible reaction, reactants are used up to form products. In the pyrolysis reaction, it is possible to observe the biomass being consumed while char, gas, and tar are generated. Due to the operational conditions that were considered in the simulation, the particle was dragged out of the fluidized reactor, which still contains a large amount of biomass to react, showing that the parameters used were not optimized. When these results are confronted with data from Papadikis et al. [11], a good approximation is observed.

2. Design of Numerical Experimets

Although the proposed model does not present a Bi<0.1, a good agreement was observed with the results of the relative yield of the pyrolysis reaction and the biomass conversion (objective of the analysis) when compared with the results of Papadikis et al. [11]. Due to the modeling complexity, the present work considers the error of 9.13% in the mass behavior and 7.63% in the residence time acceptable and therefore considers the model validated.

Following the factorial design of type 2^k, the scenarios established in Table 3 were simulated. The conversion of biomass into products was obtained as a response. The results of each scenario are shown in Table 5.

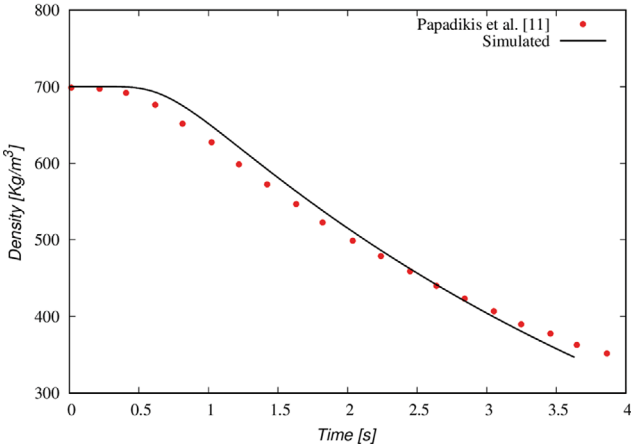

Fig. 6. Particle density behavior during pyrolysis.

When analyzing Table 5 it is observed that the best result was scenario 1, in which the highest biomass conversion into products was obtained. In this scenario, the high temperature accelerated the pyrolysis reaction, and the larger particle diameter made it difficult to drag. As a result, the biomass was consumed as much as possible, leaving with only 8.98% of the initial mass.

The difference between Simulation 1 and Simulation 2 is the particle diameter size. In scenario 1, the particle diameter generated greater resistance to drag, allowing the reaction to endure for a time of 2.71 seconds, while in scenario 2, the particle had a smaller diameter and, consequently, lower resistance to drag, being taken out of the reactor in just 0.53 seconds, affecting the biomass conversion by approximately 59.67%. As both simulations were performed with the same thermal model, the difference between residence times can be compared.

When comparing simulations 1 and 5, it is verified that the velocity's increment represented a rise in biomass conversion, even with

Table 5. Simulation results evaluated by factorial design 2^k

Scenario	u_g [m/s]	T_g [K]	d_p [m]	X_b [%]	t [s]
1	1.4	823	7.5e-4	91.02	2.71
2	1.4	823	2.5e-4	31.35	0.53
3	1.4	723	7.5e-4	14.09	>4.00
4	1.4	723	2.5e-4	01.66	0.50
5	1.0	823	7.5e-4	79.27	3.34
6	1.0	823	2.5e-4	66.49	1.44
7	1.0	723	7.5e-4	17.98	>4.00
8	1.0	723	2.5e-4	20.04	>4.00
C.B.	1.2	773	5.0e-4	47.95	3.63

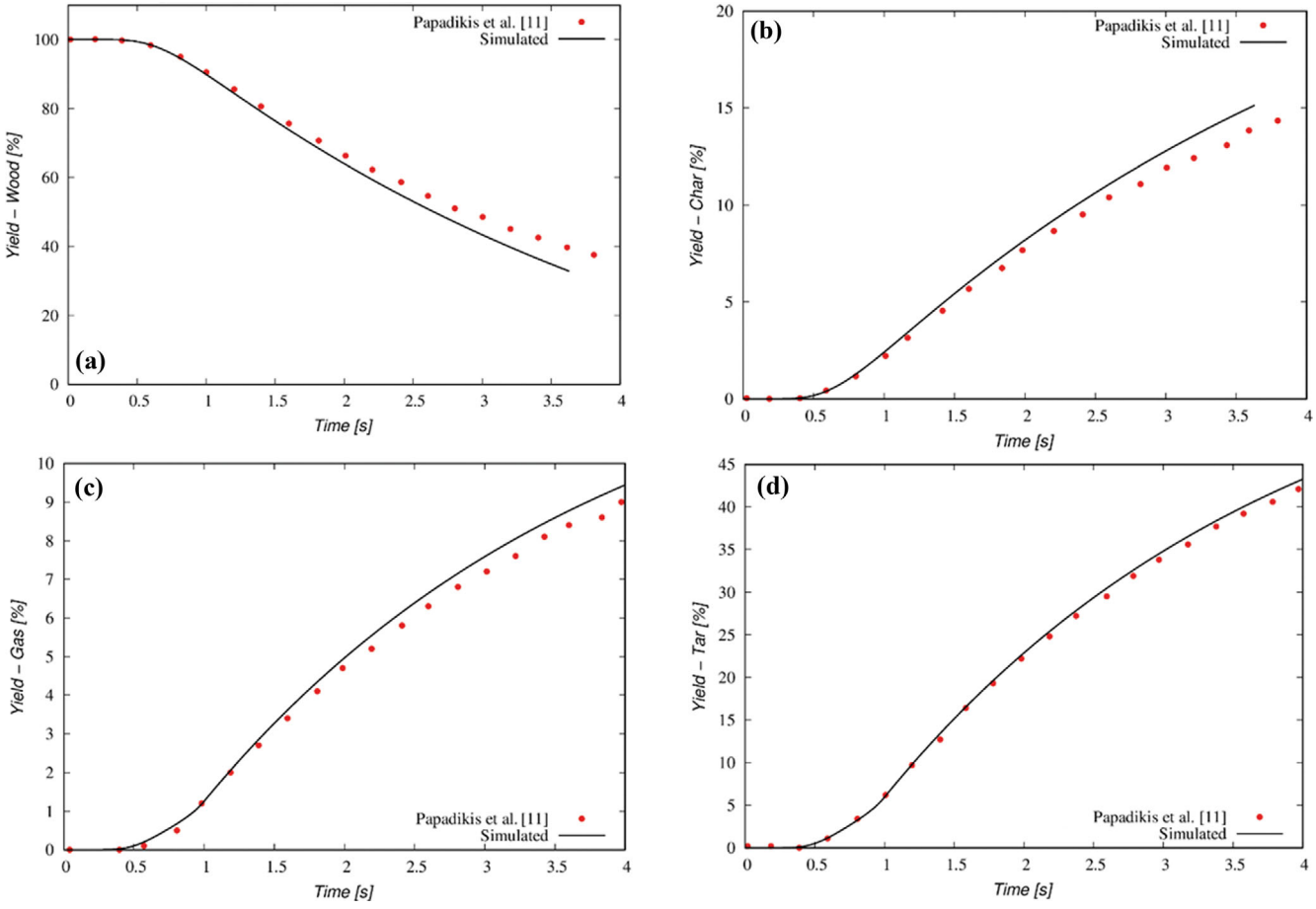

Fig. 7. Yield of (a) biomass, (b) char, (c) gas, and (d) tar during pyrolysis.

the particle remaining in the reactor for less time than in the lower velocity scenario. It is due to the higher convective heat transfer coefficient around the particle, which is generated by the high velocity that leads to the lower resistance to heat transfer.

When comparing scenarios 1 and 3, it is possible to verify that the temperature strongly influences biomass conversion value. For case 1, where the temperature is 823 K, we have a 91.02% conversion. For scenario 3, where the temperature is 723 K, and the other parameters are the same as case 1, we have a 14.09% conversion.

It is also observed that all simulations with temperatures of 723 K presented the worst conversion values, even with the longest residence times. The only exception in residence time was scenario 4, which has high velocity and small diameter, a configuration that caused the particle to be quickly dragged out of the reactor. Benevides [34] remarks that when biomass is heated in an inert atmosphere, the large and complex chains of hydrocarbons will decompose into smaller and simpler molecules. Therefore, high temperature causes easier and faster breaking of the biomass's chemical bonds.

The standardized Pareto chart for each of the individual effects and their interactions was plotted in Fig. 8, making it possible to analyze how each parameter influences biomass conversion.

Among the analyzed effects, it can be concluded from the graph shown in Fig. 8 that the inert gas temperature has significantly influenced biomass conversion. This result agrees with the behavior observed in Table 5, which shows that biomass conversion is also low when the temperature is low.

The effects, except temperature, and their interactions present a very similar influence on biomass conversion, except for the interaction between gas temperature and velocity, which is practically null. They have a biomass conversion much smaller than temperature. The graphs of the main effects (Fig. 9) and the charts of the

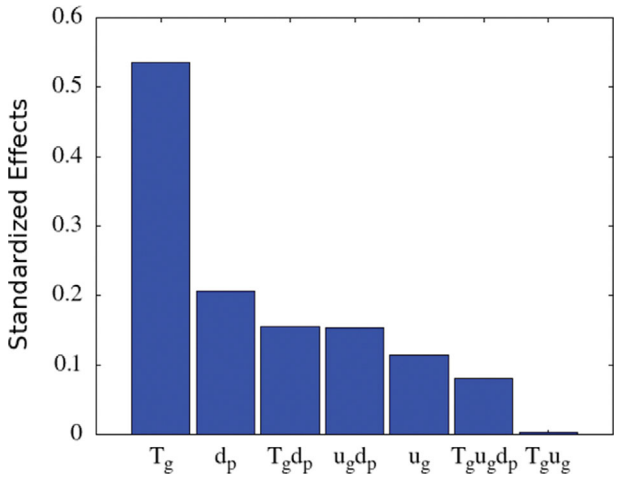

Fig. 8. Chart of standardized effects.

interactions of the effects (Fig. 10) were plotted to understand how each effect acts on the response variable.

We can understand how each parameter influences biomass conversion from the main effects graph. By observing only the behavior of the inert gas velocity, we can conclude that a velocity increase will reduce the value of biomass conversion. That occurs because the velocity increase tends to favor the drag force acting on the particle, causing it to be dragged out of the reactor more quickly and, consequently, reacting less.

When analyzing the effect of temperature on biomass conversion, as observed in Fig. 9, this parameter strongly influences the conversion. The reaction is very slow for a temperature of 723 K, reaching only 12% of it. By raising the temperature to 823 K, the con-

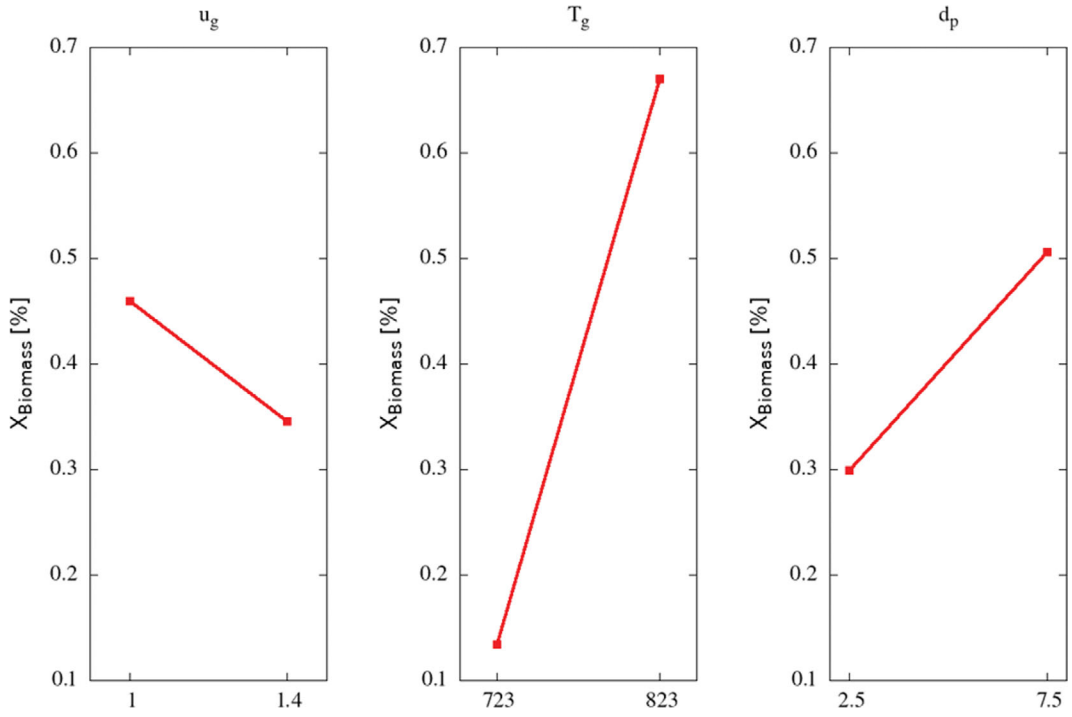

Fig. 9. Chart of individual effects.

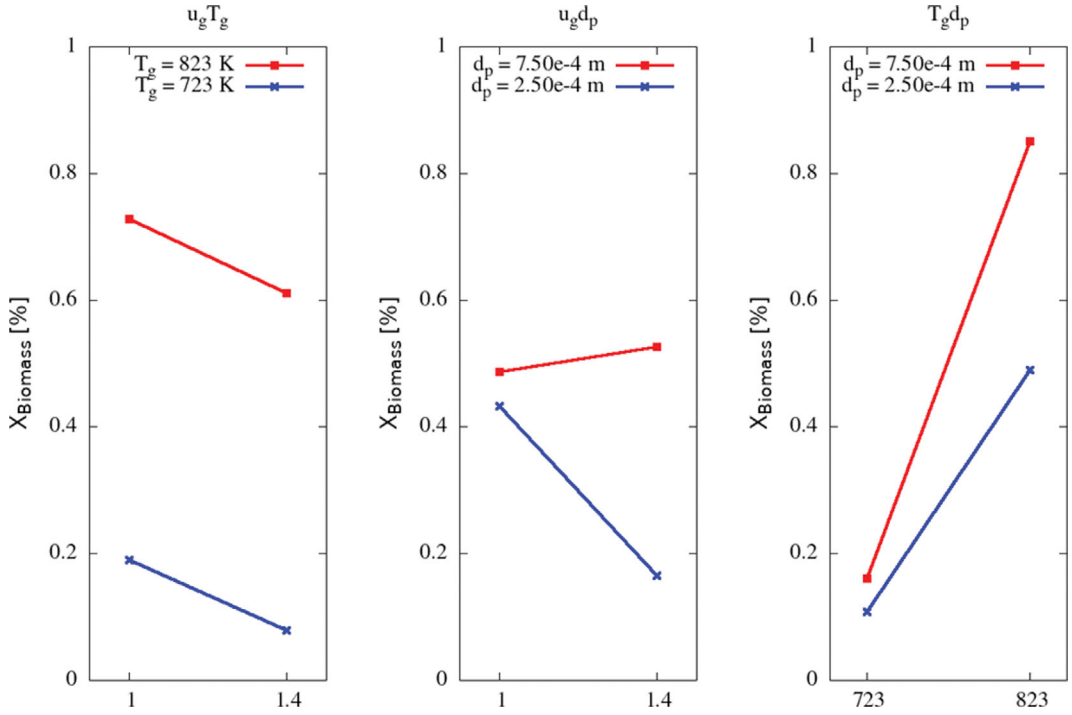

Fig. 10. Effect interaction graph.

version jumped to approximately 70%. This behavior confirms the results presented and discussed in Table 5 and Fig. 8.

By exploring the behavior of the particle diameter in Fig. 9, we found that its increment positively influences biomass conversion. Increasing the diameter of the particle means increasing its volume and, consequently, it's mass. Therefore, the drag force that previously acted on the smaller diameter particle will not be enough to drag it out of the pyrolysis reactor. That will only occur when the particle loses mass and volume during the reaction.

The effect interaction graph shows how the parameters together influence biomass conversion.

As previously discussed, the velocity interaction with the temperature observed that biomass conversion is reduced with the increment of velocity for both curves. This condition causes the particles to be carried out of the reactor more quickly due to the increased drag force. By fixing the velocity, the graph shows an increment in biomass conversion when the temperature is raised, a result that was also observed and discussed earlier. As both lines show the same trend, it can be concluded that there is no influence on biomass conversion due to the interaction of velocity with temperature, confirming the result presented in Fig. 8.

The curves' behavior in the interaction between the velocity and the diameter of the particle are opposites. The biomass conversion slightly increases when the velocity increases for the diameter of 7.50×10^{-4} m, while for the diameter of 2.50×10^{-4} m, the conversion suffers a substantial reduction. That occurs because the increased velocity of small particles causes them to be dragged out of the reactor. On the other hand, by increasing the velocity and the diameter, the particle's weight compensates for the increased drag force, causing the particles to be carried less easily out of the reactor. The increment in conversion in the latter case is due to the rise in velocity around the particle, which facilitates heat transfer by the convection mechanism.

In the interaction of particle diameter with temperature, an biomass conversion increment is observed when the temperature is high. However, for the smaller diameter scenario, the difference between conversions is slight when compared to the larger diameter scenario, showing that there is an influence when these two quantities are coupled. During pyrolysis, the particle is converted into gas and tar, losing mass until it does not resist the drag force and is taken out of the reactor. When we increase the diameter and raise the temperature, the particle will have a greater mass and consequently will offer greater resistance to the drag force than smaller particles, spending more time inside the reactor at high temperatures and achieving greater conversions.

CONCLUSION

Based on the numerical simulation, the following conclusions can be drawn:

(a) When comparing the results obtained from the lumped capacitance thermal model with the results from the discretization model reported in the literature, an error of 9.13% was observed in the particle mass behavior, and an error of 7.63% was observed in its residence time in the reactor.

(b) The lumped capacitance thermal model accurately represented the behavior of reactant and product yields for particles with a Biot number of 0.24. It can be considered a good approximation for studies involving a large number of particles, as the thermal discretization model incurs a high computational cost.

(c) The results obtained from the experimental design study showed consistent results, indicating that the highest biomass con-

version value was obtained among the evaluated scenarios when the highest speed, temperature, and particle diameter were simulated.

(d) The results from the Design of Experiments (DoE) indicate that the gas temperature is the parameter that most significantly influences biomass conversion. In contrast, the other parameters and their interactions do not have a significant impact on the conversion rate.

NOMENCLATURE

u : velocity vectors [m/s]
p : pressure [Pa]
g : gravity acceleration [m/s^2]
F : momentum source term [kg/m^{2}s^2]
C : Smagorinsky's constant [ ]
h : enthalpy [J/kg]
q : conduction heat flow [W/m^3]
Q : heat [W/m^3]
Y : mass fraction [ ]
c_p : heat capacity [J/kg K]
N : chemical species number
h_c : convection heat transfer coefficient [W/m^{2}K]
N_u : Nusselt number [ ]
T : temperature [K]
L : characteristic length [m]
B_i : biot number [ ]
P_r : Prandtl number [ ]
D_{if} : mass diffusivity [m^2/s]
S_c : Schmidt number [ ]
f : force [N]
m : mass [kg]
I : moment of inertia [kg m^2]
M : torque [N m]
r : radius [m]
d : diameter [m]
A : surface area [m^2]
V : volume [m^3]
R_e : Reynolds number [ ]
C_d : drag coeficient [ ]
E : activation energy [J/kmol]
R : universal gas constant [8.31 J/mol K]
k : reaction rate [s^{-1}]
t : time [s]
X : conversion rate [%]
τ : stress tensor [Pa]
α : phase volume fraction [ ]
μ : dynamics viscosity [Pa s]
γ : pre-exponential factor [s^{-1}]
σ : Stefan-Boltzmann constant [5.6697×10^{-8} W/m^{2}K^4]
ε : emissivity [ ]
Ω : reaction [kg/m^3 s]
ΔH_r : heat of reaction
λ : thermal conductivity [W/m K]

Subscripts

g : gas
s : solid
p : particle
b : biomass
gs : gas-solid interaction
l : Laminar
t : Turbulent
k : chemical species
gw : gas-wall interaction
w : wall
react : reaction
i : particle i
rad : radiation
b : boundary
d : drag
0 : initial

Superscript

K : chemical species
g-s : gas-solid interaction
s-w : gas-wall interaction
grav : gravitational

REFERENCES

1. J. Clissold, S. Jalalifar, F. Salehi, R. Abbassi and M. Ghodrat, *Fuel*, **273**, 117791 (2020).
2. S. Hameed, A. Sharma, V. Pareek, H. Wu and Y. Yu, *Biomass Bioenerg.*, **123**, 104 (2019).
3. S. Vikram, P. Rosha and S. Kumar, *Energy Fuels*, **35**(9), 7406 (2021).
4. S. Sobek and S. Werle, *Renew. Energy*, **143**, 1939 (2019).
5. A. Sharma, V. Pareek and D. Zhang *Renew. Sust. Energ. Rev.*, **50**, 1081 (2015).
6. S. Yang, Z. Wan, S. Wang and H. Wang, *J. Environ. Chem. Eng.*, **9**(2), 105047 (2021).
7. C. R. Duarte, I. P. Junior and D. A. dos Santos, in Horizonte Científico (2015).
8. B. Hooshdaran, M. Haghshenasfard, S. H. Hosseini, M. N. Esfahany, G. Lopez and M. Olazar, *J. Anal. Appl. Pyrol.*, **154**, 105011 (2021).
9. K. Papadikis, H. Gerhauser, A. Bridgwater and S. Gu, *Biomass Bioenerg.*, **33**(1), 97 (2009).
10. K. Papadikis, S. Gu and A. Bridgwater, *Chem. Eng. J.*, **149**(1), 417 (2009).
11. K. Papadikis, S. Gu, A. Bridgwater and H. Gerhauser, *Fuel Process. Technol.*, **90**(4), 504 (2009).
12. K. Papadikis, S. Gu and A. Bridgwater, *Fuel Process. Technol.*, **91**(7), 749 (2010).
13. K. Papadikis, S. Gu and A. Bridgwater, *Fuel Process. Technol.*, **91**(1), 68 (2010).
14. C. Hu, K. Luo, S. Wang, L. Sun and J. Fan, *Ind. Eng. Chem. Res.*, **58**(3), 1404 (2019).
15. H. C. Park and H. S. Choi, *Renew. Energy*, **143**, 1268 (2019).
16. J. Smagorinsky, *Monthly Weather Rev.*, **91**(3), 99 (1963).
17. S. Ergun and A. A. Orning, *Ind. Eng. Chem.*, **41**(6), 1179 (1949).
18. S. Yang, Z. Wan, S. Wang and H. Wang, *J. Environ. Chem. Eng.*, **9**(2), 105047 (2021).

19. M. Bashir, X. Yu, M. Hassan and Y. Makkawi, *ACS Sustainable Chem. Eng.*, **5**(5), 3795 (2017).
20. J. E. Lee, H. C. Park and H. S. Choi, *ACS Sustainable Chem. Eng.*, **5**(3), 2196 (2017).
21. S. Maduskar, G. G. Facas, C. Papageorgiou, C. L. Williams and P. J. Dauenhauer, *ACS Sustainable Chem. Eng.*, **6**(1), 1387 (2018).
22. J. Clissold, S. Jalalifar, F. Salehi, R. Abbassi and M. Ghodrat, *Fuel*, **273**, 117791 (2020).
23. S. Yang, R. Dong, Y. Du, S. Wang and H. Wang, *Energy*, **214**, 118839 (2021).
24. W.-C. R. Chan, M. Kelbon and B. B. Krieger, *Fuel*, **64**(11), 1505 (1985).
25. T. Li, P. Gopalakrishnan, R. Garg and M. Shahnam, *Particuology*, **10**(5), 532 (2012).
26. H. K. Versteeg and W. Malalasekera, *An introduction to computational fluid dynamics*, Harlow: Pearson Prentice Hall (2007).
27. C. Hu, K. Luo, S. Wang, L. Sun and J. Fan, *Ind, Eng. Chem. Res.*, **58**(3), 1404 (2019).
28. Z. Peng, E. Doroodchi, C. Luo and B. Moghtaderi, *AIChE J.*, **60**(6), 2000 (2014).
29. D. Clarke, A. Sederman, L. Gladden and D. Holland, *Ind. Eng. Chem. Res.*, **57**(8), 3002 (2018).
30. C. Boyce, D. Holland, J. Dennis and S. Scott, *Ind. Eng. Chem. Res.*, **54**(43), 10684 (2015).
31. Q. Xiong, S.-C. Kong and A. Passalacqua, *Chem. Eng. Sci.*, **99**, 305 (2013).
32. H. R. Norouzi, R. Zarghami, R. SotudehGharebagh and N. Mostoufi, *Elsevier*, **1**(1), 269 (2019).
33. R. Batista Junior, Master's thesis, UFTM (2017).
34. L. C. Benevides, Master's thesis, UFES, (2015).